OPTICS

Spatially entangled photon pairs from lithium niobate nonlocal metasurfaces

Jihua Zhang[1]†, Jinyong Ma[1]†, Matthew Parry[1], Marcus Cai[1], Rocio Camacho-Morales[1], Lei Xu[2], Dragomir N. Neshev[1], Andrey A. Sukhorukov[1]*

Metasurfaces consisting of nanoscale structures are underpinning new physical principles for the creation and shaping of quantum states of light. Multiphoton states that are entangled in spatial or angular domains are an essential resource for many quantum applications; however, their production traditionally relies on bulky nonlinear crystals. We predict and demonstrate experimentally the generation of spatially entangled photon pairs through spontaneous parametric down-conversion from a metasurface incorporating a nonlinear thin film of lithium niobate covered by a silica meta-grating. We measure the correlations of photon pairs and identify their spatial antibunching through violation of the classical Cauchy-Schwarz inequality, witnessing the presence of multimode entanglement. Simultaneously, the photon-pair rate is strongly enhanced by 450 times as compared to unpatterned films because of high-quality-factor resonances. These results pave the way to miniaturization of various quantum devices by incorporating ultrathin metasurfaces functioning as room temperature sources of quantum-entangled photons.

INTRODUCTION

Quantum entanglement underpins a broad range of fundamental physical effects (*1*) and serves as an essential resource in various applications including quantum imaging (*2*), communications (*3*), information processing, and computations (*4*). In optics, the most common source of entangled photons is based on the spontaneous parametric down-conversion (SPDC) process in quadratically nonlinear materials (*5*), which can operate at room temperature. The generated photons can be entangled in transverse (*6*, *7*) and orbital angular momenta (*8*), effectively accessing a large Hilbert space (*9*–*11*). Strong transverse momentum entanglement was recently realized with a micrometer-scale film of nonlinear material lithium niobate ($LiNbO_3$) (*12*), yet the compactness came at a cost of a strongly reduced generation rate. This leads to a fundamentally and practically important research question on the potential for efficient generation of spatially entangled photons in ultrathin optical structures.

Over the past decade, marked enhancements of nonlinear light-matter interactions were achieved in nanofabricated structures with subwavelength thickness, known as metasurfaces (*13*, *14*), which are also bringing advances to the field of quantum optics (*15*). An enhancement of SPDC through localized Mie-type optical resonances (*16*) in nanoantennas (*17*) and metasurfaces (*18*) was experimentally demonstrated. Recent theoretical studies (*19*–*21*) suggested that using metasurfaces with nonlocal lattice resonances (*22*, *23*) can further boost the SPDC efficiency, yet the realization of this concept remained outstanding.

In this work, we demonstrate experimentally, that strongly enhanced generation of spatially entangled photon pairs can be achieved from metasurfaces supporting nonlocal resonances at the signal and idler in the telecommunication band around the 1570-nm wavelength. The SPDC enhancement of ~450 times compared with unpatterned film and the coincidence-to-accidental ratio (CAR) of ~5000 are an order of magnitude higher than what has been possible to date (*18*), benefiting from the nonlocal feature of the resonances. This is the foundation for the preparation of strongly entangled quantum states with a much higher spectral and spatial brightness compared to localized resonances. Our experiments indicate spatial entanglement of photon pairs by violating the classical Cauchy-Schwarz inequality (CSI), confirming the practical path for the preparation of high-quality entanglement sources with metasurfaces.

RESULTS

Concept and modeling

We develop a nonlocal metasurface based on the $LiNbO_3$-on-insulator platform, which was recently used for various applications including electro-optic modulation (*24*, *25*) and classical optical frequency conversion (*26*). The $LiNbO_3$ material features large second-order susceptibility, low fluorescence, and high optical transmission in a broad wavelength range (*27*, *28*), which are essential for the quality of generated photon pairs. We design a periodic SiO_2 grating on top of a lithium niobate film with subwavelength thickness ($t \simeq 304$ nm), as schematically illustrated in Fig. 1A.

We select the x cut of $LiNbO_3$ and orient the grating along the z axis of the film, such that the efficiency of SPDC is maximized when the pump beam and emitted photons are linearly polarized along the z axis, because of its highest nonlinear tensor coefficient $\chi^{(2)}_{zzz}$. Note that this design does not require nanopatterning of the $LiNbO_3$ film, in contrast to Mie-resonant metasurfaces (*18*), thereby avoiding possible damage at the edges while preserving the total volume of the nonlinear material.

The grating supports guided-mode resonances inside the $LiNbO_3$ layer when the transverse wave number determined by the incident wave and the grating matches the propagation wave number of the slab modes (*29*–*31*). This physical mechanism underpins a strongly nonlocal response since the resonant excitations can spread out in-plane through the guided waves (*32*–*34*). Mathematically, the nonlocality in space is intrinsically linked to the presence of angular

[1]ARC Centre of Excellence for Transformative Meta-Optical Systems (TMOS), Research School of Physics, The Australian National University, Canberra, ACT 2601, Australia. [2]Advanced Optics and Photonics Laboratory, Department of Engineering, School of Science and Technology, Nottingham Trent University, Nottingham NG11 8NS, UK.
†Co-first authors with equal contribution.
*Corresponding author. Email: andrey.sukhorukov@anu.edu.au

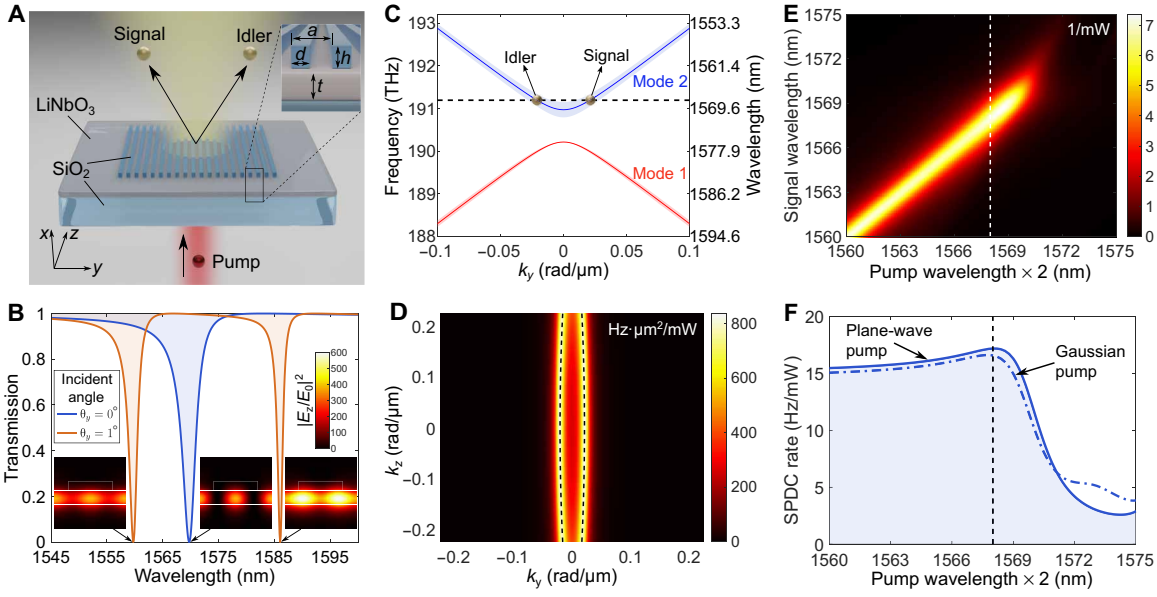

Fig. 1. Nonlocal metasurfaces for efficient generation of spatially entangled photon pairs. (**A**) Sketch of spatially entangled signal and idler photon generation from a $LiNbO_3$ thin film covered by an SiO_2 grating and pumped by a continuous laser. The optical axis of $LiNbO_3$ and the grating are along the *z* direction. Inset shows the dimensions of the metasurface (not to scale), which we choose as $a = 890$ nm, $d = 550$ nm, $h = 200$ nm, and $t = 304$ nm. (**B**) Simulated transmission spectra of the metasurface for *z*-polarized light, showing a single guided-mode resonance at normal incidence and two resonances with a nonzero incident angle. This angular dependent transmission features a nonlocal response. The insets are the field intensity at the resonances, showing strong field enhancement in the $LiNbO_3$ layer. (**C**) Simulated eigenfrequencies of resonances versus the transverse wave number k_y at $k_z = 0$. The shaded regions represent the bandwidth of the resonances. Signal and idler photons produced symmetrically relative to the Γ point satisfy both the energy and transverse momentum conservation, when half the pump frequency ω_p is within the resonance range. The black dashed line marks $\omega_p/2 = 191.19$ THz, which is slightly blue-detuned from the normal incidence resonance of the bright mode 2. (**D**) Predicted photon emission rate at the marked pump frequency as a function of transverse wave numbers. The black dashed line indicates the momentum matching conditions for the degenerate SPDC. (**E**) Spectra of the signal photons for different pump frequencies. (**F**) The total emission rate after integrating over the signal spectrum for plane-wave and Gaussian (100-μm-diameter) pump beam. The vertical dashed lines in (E) and (F) relate to the pump frequency marked in (C).

dispersion. We first discuss the key features by considering a case of the incident plane wave wherein transverse wave number along the grating is vanishing, i.e., $k_z = 0$. In the weak-grating regime, which does not exactly apply to metasurfaces yet captures the essential physics, the first-order resonance happens when the following condition is satisfied (*35*, *36*)

$$\frac{2\pi}{a} \pm \sin\theta_y \frac{2\pi}{\lambda} = n_{\text{eff}} \frac{2\pi}{\lambda} \quad (1)$$

where a is the period of the grating, θ_y is the incident angle of the input plane wave in the *y*-*x* plane, λ is the wavelength in vacuum, n_{eff} is the effective index of the waveguide mode in the $LiNbO_3$ film, and the sign ± corresponds to the two guided modes propagating in opposite directions along the *y* axis. Equation 1 indicates the presence of two resonant wavelengths at $\lambda = a(n_{\text{eff}} \pm \sin\theta_y)$, which depend on the incident angle and can be controlled by selecting the period of the grating.

We determine an approximate grating period for the target photon-pair wavelengths in the telecommunication band using Eq. 1 and then fine-tune the structure parameters by performing finite-element modeling of Maxwell's equations to also facilitate electromagnetic field localization inside the $LiNbO_3$ layer. The optimized geometry is sketched in the inset of Fig. 1A. We present the characteristic transmission spectra in Fig. 1B at normal and tilted incidence as indicated by labels and show the dependencies of the resonant eigenfrequencies (ω) and bandwidths defined by the loss coefficients (2γ) of the quasi-normal modes on the transverse wave numbers along the *y* axis in Fig. 1C. The corresponding quality factors of the resonances are $Q = \omega/(2\gamma)$.

Let us first analyze the mode features at the Γ point, i.e., $k_y = 0$. There is a small frequency splitting because of a second-order grating scattering that is not captured by simplified Eq. 1. The lower-frequency mode 1 has zero bandwidth and thus an infinite quality factor. We check that this mode has an antisymmetric electric field profile (see fig. S1), indicating its origin as a symmetry-protected extended bound state in the continuum (BIC) (*37*). The single resonant transmission dip at normal incidence (Fig. 1B) corresponds to an excitation of a bright mode 2, which has a quality factor of ≃500. As shown in the inset, the mode has a symmetric standing-wave intensity profile because of the interference of equally excited counterpropagating guided modes.

For an incident angle of 1°, with $k_y \simeq 0.07$ rad/μm, two transmission dips appear at both sides of the resonance at $k_y = 0$. The weakly modulated intensity profiles shown in the insets of Fig. 1B indicate the dominance of one guided mode, in agreement with the general properties of lattice resonances. For both modes 1 and 2, a strong intensity enhancement of up to 600 times is observed inside the $LiNbO_3$ layer, which can accordingly increase the efficiency of the nonlinear processes including second harmonic generation (SHG) and SPDC as we demonstrate in the following.

The high Q-factors are retained for a broad range of incidence angles, while the two resonance frequencies move further apart for

the larger values of $|k_y|$. This dispersion dependence defines the group velocity of the quasi-guided modes in the lithium niobate layer, $v_g = \partial\omega/\partial k_y$. Noting that the characteristic mode lifetime where the intensity decreases by a factor of 2 can be found as $\tau \simeq \ln(2)/(2\gamma) = \ln(2)Q/\omega$, we estimate the propagation distance in the y direction of the quasi-guided mode 2 at $k_y \simeq 0.07$ rad/μm as $\tau v_g \simeq 71$ μm. The latter value represents approximately 80 grating periods, confirming a strongly nonlocal nature of the metasurface resonances.

In addition to the high-quality resonances, both the energy and transverse momentum conservation conditions need to be satisfied in the SPDC process of photon-pair generation. We designed the meta-grating to satisfy an in-plane symmetry $y \rightarrow -y$, such that the resonances at k_y and $-k_y$ appear at the same frequency. This property allows the simultaneous fulfillment of phase and energy matching of a spectral-degenerate SPDC process when the half-frequency of a normally incident pump is in the guided mode resonance range. For example, the black dashed line in Fig. 1C corresponds to a pump frequency $\omega_p = 2 \times 191.19$ THz. Accordingly, the frequency of the resonantly enhanced signal and idler photons and their emission angles can be controlled by tuning the pump frequency, which allows one to tailor the spectrum and spatial entanglement of the photon pairs.

The SPDC emission can occur over a range of transverse momenta and photon frequencies, and accordingly, the associated quantum biphoton states belong to a high-dimensional Hilbert space. Their modeling requires fast and accurate simulation methods. For this purpose, we adopt a coupled mode theory (CMT) (*38*, *39*) approach to our metasurface design and verify that it precisely describes the metasurface resonances, including all the angular and frequency features (see section S1). We then use the CMT to efficiently simulate the sum frequency generation (SFG) process and calculate the SPDC emission via quantum-classical correspondence (*17*, *19*). Figure 1D shows the predicted photon-pair rate integrated over their frequency spectra versus the transverse momenta in the metasurface plane, for a normally incident plane-wave pump with the frequency $\omega_p = 2 \times 191.19$ THz. The elongated emission pattern in the z direction reflects a weak quadratic dispersion dependence on k_z (see fig. S2). We mark with the black dashed line the transverse phase-matching condition at the center of mode resonances, which aligns with the emission peaks.

We present the dependence on the pump frequency of the photon spectra integrated over all emission angles in Fig. 1E and the total emission rate in Fig. 1F. Here, the frequency range corresponding to the excitation of mode 2 is shown, while similar features are observed for mode 1 away from the band edge, where tunable off-normal photon emission can be achieved. The vertical dashed lines correspond to the pump frequency $\omega_p = 2 \times 191.19$ THz, at which the highest total rate is predicted. The corresponding degenerate photon frequencies are slightly blue-detuned from the bright mode 2 resonance at normal incidence, since in the latter case, the Q-factor is lower and quadratic band-edge dispersion affects the phase matching. We find that the SPDC rate can be enhanced by over two orders of magnitude compared with an unpatterned $LiNbO_3$ film of the same thickness, with an even stronger increase in spectral brightness (see fig. S4). The enhancement is preserved under the practical experimental conditions of a Gaussian beam pump rather than an idealized plane wave, as shown in Fig. 1F.

It is a remarkable feature that the enhanced photon rate stays practically constant as the pump wavelength is decreased. The tuning range of the signal and idler wavelengths, determined by twice the pump wavelength, can be up to hundreds of nanometers without temperature adjustment. These properties are facilitated by the nonlocal metasurface resonances, in which dispersion also mediates the tunability of the emission angles, offering great flexibility for future applications.

Experimental characterization: Metasurface resonances and enhanced SHG

We fabricate the metasurface by electron beam lithography and etching processes as described in Materials and Methods. The scanning electron microscopy (SEM) image of the meta-grating is shown in Fig. 2A, which confirms that the dimensions closely match the optimal design geometry according to our theoretical analysis. The experimental transmission measurements (Fig. 2B and fig. S6) of the metasurface identify a resonance at 1570.5 nm with a bandwidth of 3.5 nm and a quality factor $Q \sim 455$, for a normally incident light. Note that another shallow dip at 1580 nm corresponding to the dark mode 1 resonance is also visible at normal incidence, because the white light source has a finite angular range, and fabrication imperfections break the symmetry and transform the mode into a quasi-BIC one. Two resonances with a visible spectral splitting manifest at a nonzero incidence angle. The observed angular dispersion confirms the nonlocal origin of resonances in agreement with the theoretical modeling presented above.

The classical nonlinear effects, SHG and SFG, can be regarded as the reverse processes of the SPDC (*17*, *19*). It was recently established that SHG and SFG can occur in $LiNbO_3$ thin films (*40*, *41*) and can be enhanced in metasurfaces with Mie-type resonances (*42*–*45*). Here, we test the nonlinearity enhancement by exploring the SHG from the nonlocal metasurface, using the experimental setup sketched in Fig. 2C. The SHG is triggered with a femtosecond laser whose central wavelength is tunable from 1540 to 1580 nm. In all SHG experiments, the laser is normally incident onto the sample from the grating side.

We compare the efficiency of the SHG from the metasurface and unpatterned film in Fig. 2D and register up to 50 times the enhancement. For both cases, the polarization of the incident laser is oriented along the z axis of the nonlinear film to make use of the highest nonlinear tensor coefficient $\chi^{(2)}_{zzz}$ and maximize the SHG efficiency. Note that the pulsed laser bandwidth is 23 nm, which is larger than the linewidth of the metasurface resonances, significantly limiting the measured enhancement. In addition, we characterize the SHG enhancement by laser pulses with different central wavelengths (see Fig. 2E). The optimal enhancement is observed when the pulse central wavelength sits within the bright-mode resonance of the metasurface. These results confirm the high quality of the fabricated metasurfaces, which strongly boost nonlinear wave mixing in the $LiNbO_3$ layer because of nonlocal resonances according to our theoretical concept.

Quantum measurements: Enhanced photon-pair generation and spatial entanglement

We now proceed with the experimental investigations of the quantum photon-pair generation. A setup sketch for characterizing the SPDC is shown in Fig. 3A. The metasurface is pumped with a continuous-wave laser tunable around the 785-nm wavelength with a beam diameter of ~100 μm. The correlations of photon pairs generated from the metasurface are analyzed with a Hanbury Brown–Twiss

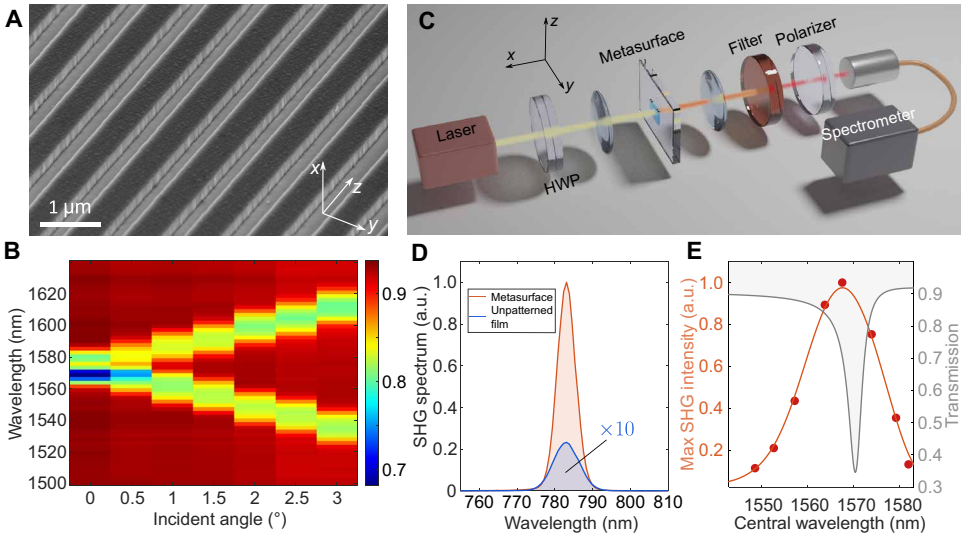

Fig. 2. Classical experiment: Linear transmission and enhanced SHG of the nonlocal metasurface. (**A**) SEM image of the fabricated dielectric meta-grating on top of an *x*-cut 304-nm-thick lithium niobate film. (**B**) Measured linear transmission as a function of incident angle and wavelength. The resonance is nearly degenerate at normal incidence and shows a mode splitting at a larger angle. The transmission is measured with a tungsten-halogen broadband lamp. (**C**) Experimental setup for SHG. The metasurface is pumped with femtosecond laser pulses from the grating side, with a tunable central wavelength and a bandwidth of 23 nm. The SHG signal is collected with a spectrometer. (**D**) SHG spectra from metasurface (red curve) and unpatterned film (blue curve). The SHG intensity is normalized to its maximum from the metasurface. (**E**) Normalized peak SHG intensity versus the central wavelength of the input pulses. The shaded gray curve shows the Fano fitting of the metasurface transmission measured with a tunable continuous-wave laser (1500 to 1575 nm) at normal incidence (see fig. S6). This measurement shows a narrower band but a higher resolution as compared with the results obtained from the lamp. The red dots are maximum SHG intensity extracted from SHG spectra obtained at different pulsed laser central wavelengths, and the red line is the corresponding spline fitting. The optimal enhancement is found near the optical resonance. a.u., arbitrary units.

setup, using a 50:50 multimode fiber beam splitter and two single-photon detectors based on InGaAs/InP avalanche photodiodes (see Materials and Methods).

The measured coincidences of photon pairs from the metasurface for different time delays between the detectors are displayed in Fig. 3B. We obtain a coincidence rate of 1.8 Hz at a pump power of 85 mW, corresponding to a photon generation efficiency of 21 mHz/mW. The efficiency of single-photon detectors calibrated by the manufacturer is 25%, and the collection efficiency for each photon is estimated as 25 to 30%, which results in an overall detection efficiency of 0.4 to 0.6% for the photon pairs. This suggests a photon-pair emission rate of 2.3 to 3.5 Hz/mW from the metasurface over a collection angle range calibrated as ~0. 7°, which closely agrees with the theoretical predictions (see fig. S3C).

For comparison, we also measure the photon-pair rate from an unpatterned $LiNbO_3$ film under the same experimental conditions, which is found to be 0.047 mHz/mW at zero delay. On the basis of the peak values of the histograms shown in Fig. 3B, we identify a rate enhancement of 450 times from the metasurface compared to an unpatterned film, which agrees with the numerical modeling (see fig. S4B). Our theory also predicts that the generated photon pairs have a narrow bandwidth of ~3 nm, and the spectral brightness enhancement at the central wavelength is ~1400 times (see fig. S4A).

We confirm that the measured coincidences can be attributed to the generation of nonclassical photon pairs by analyzing the second-order correlation function $g^{(2)}(0)$. For the resonantly enhanced emission from the metasurface, $g^{(2)}(0)$ reaches the value of ~5000 (see fig. S8A). The corresponding coincidence to accidental ratio (CAR = $g^{(2)}(0) - 1$) is ~ 5000, which is over three orders of magnitude larger than the classical bound of 2. Both the measured rate enhancement and CAR in our metasurface, which are independent of the detector and collection efficiencies, are an order of magnitude higher than previously reported for photon-pair generation from nonlinear metasurfaces with localized Mie resonances (*18*). These enhanced rates are the foundation for the preparation of strongly entangled quantum states with a much higher spectral and spatial brightness (*19*, *21*) compared to localized resonances.

The SPDC efficiency is expected to nontrivially depend on the pump wavelength, reflecting the pronounced dispersion of the nonlocal metasurface resonances. We collect the real coincidence (total peak coincidence with subtracted accidental coincidences) for different pump wavelengths, as shown in Fig. 3C (red dots with error bars), where the horizontal axis indicates the degenerate signal/idler wavelength, i.e., two times of the pump wavelength. The data points are taken with different wavelength steps determined by the tuning characteristics of the pump laser (see section S2.3). The maximum coincidence is found when the degenerate wavelength is slightly blue-detuned from the bright-mode resonance at normal incidence (gray curve), which is consistent with the theoretical predictions in Fig. 1F. We fit the experimental data to the formulated CMT with two free parameters, the collection angle and overall detection efficiency. The fitting results indicate a collection angle of 0.68° and a total detection efficiency of 0.4%, which is a good match with the experimental parameters presented above.

Experimental measurements confirm that the enhanced photon-pair rate remains close to its maximum over a broad span of pump wavelengths, when the spatial emission is within the range of collection angles. This efficient spectrum tunability of photon pairs is a distinguishing feature of our metasurface with nonlocal resonances, where the transverse phase matching is satisfied for a continuous set

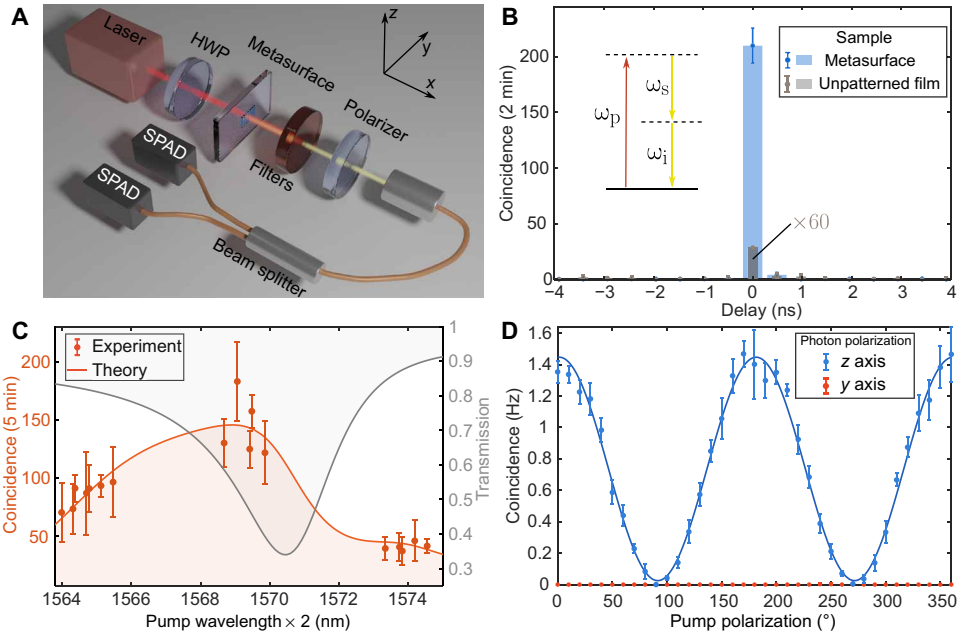

Fig. 3. Quantum experiment: Enhanced generation of photon pairs from the nonlocal metasurface. (**A**) Setup for SPDC. A laser beam with a wavelength at 785 nm is focused on a metasurface fabricated on top of a lithium niobate film to produce photon pairs. The photon pairs pass through a 50:50 fiber beam splitter, and their coincidence is then registered by two single-photon detectors. (**B**) Coincidence histograms of SPDC from metasurface (blue bar) and unpatterned film (gray bar). The gray bar is obtained via the integration time of 2 hours, which is 60 times longer than the measurement of the blue bar. (**C**) Real coincidence as a function of the degenerate signal/idler wavelength, which is two times the pump wavelength. The experiment (dots with error bars) shows a good agreement with the theoretical result (solid line). Error bars indicate 2 SD (standard deviation). The transmission curve (gray) is the same as the one given in Fig. 2E. (**D**) Real coincidence as a function of pump polarization. Points and lines are experimental results and theoretical fitting, respectively, for the photon-pair polarization along the *z* or *y* axis of the film as indicated in the inset. Error bars indicate 1 SD. The pump powers used for (B) to (D) are 85, 35, and 75 mW, respectively.

of pump wavelengths, while there are no limitations due to longitudinal phase matching in contrast to bulk nonlinear crystals.

Next, we analyze the dependence of the SPDC on the pump polarization by rotating the half-wave plate (HWP) placed before the metasurface and measuring the photon coincidences with a linear polarizer placed after the metasurface oriented in the *y* or *z* direction. We show in Fig. 3D that the real coincidence count is strongly dependent on the pump polarization when the polarizer is parallel to the *z* axis ($LiNbO_3$ optical axis); meanwhile, almost no photons are detected at any pump polarization angle when the polarizer is rotated along the *y* axis. That is, the coincidence rate is maximized when both the pump and emitted photon pairs are polarized along the *z* axis of the film, when the nonlinear wave mixing is mediated by the strongest quadratic susceptibility tensor component of $LiNbO_3$. The visibility of the polarization dependence is estimated to be above 99%, benefiting from the selective resonant enhancement of the SPDC for the photon polarizations along the grating direction according to our metasurface design.

Last, we experimentally confirm the spatial entanglement of the photon pairs by selectively blocking photons with an aperture. Such measurements allow us to reveal the presence of nonclassical correlations between the photons at different spatial regions. We use a square aperture placed after the photon emission (Fig. 4A) and translate it transversely in the *y* or *z* direction. The width of the aperture is $L = 4.5$ mm, which is chosen to be larger than the aperture of the collected photons (Fig. 4B). The real two-photon coincidences $C(q)$ as a function of the aperture position q ($q = y$ or $q = z$) are presented in Fig. 4 (C and D). Note that at $q = 0$, the center of the aperture is aligned with the center of the beam. The diameters of the collected beam d_q ($q = y, z$), which are estimated by subtracting the aperture width from the flat plateau region of the correlation curves in Fig. 4 (C and D), are $d_y = 0.55L$ and $d_z = 0.65L$, respectively.

Let us consider a counterexample of classical light correlations, which should satisfy the CSI that, for our setup, can be formulated as (see section S3)

$$\Gamma(q_s) \equiv \left(\sqrt{C(q_s - L/2)} + \sqrt{C(q_s + L/2)}\right)^2 \geq C(0) \qquad (2)$$

Here, $C(q_s - L/2)$ and $C(q_s + L/2)$ represent the two-photon coincidences within the two complementary emission regions A_1 and A_2 separated at the position q_s, as sketched in Fig. 4B. The CSI can be violated for quantum states, when $\Gamma(q_s) < C(0)$, indicating nonclassical spatial correlations and multimode spatial entanglement (*46*). The underlying physics can be interpreted as the spatial analog of the photon antibunching effect (*47*). The quantities on the left-hand side of Eq. 2 are proportional to the self-correlations within the regions A_1 or A_2 and when their quadratic combination is below the total correlations over the whole beam $C(0)$, it means that the cross-correlations between regions A_1 and A_2 are higher than what is possible classically.

We identify the violation of CSI by applying Eq. 2 to the correlation measurements from Fig. 4 (C and D) and present the values of $\Gamma(q_s)$ in Fig. 4 (E and F). For convenience, we normalize the data such that the plotted value of $C(0)$ is unity, which defines the classical bound. We see that $\Gamma(q_s)$ is significantly lower than the classical bound by over 3 standard deviations (SDs) for a broad range of spatial region boundaries, $-0.2 < q_s/L < 0.2$.

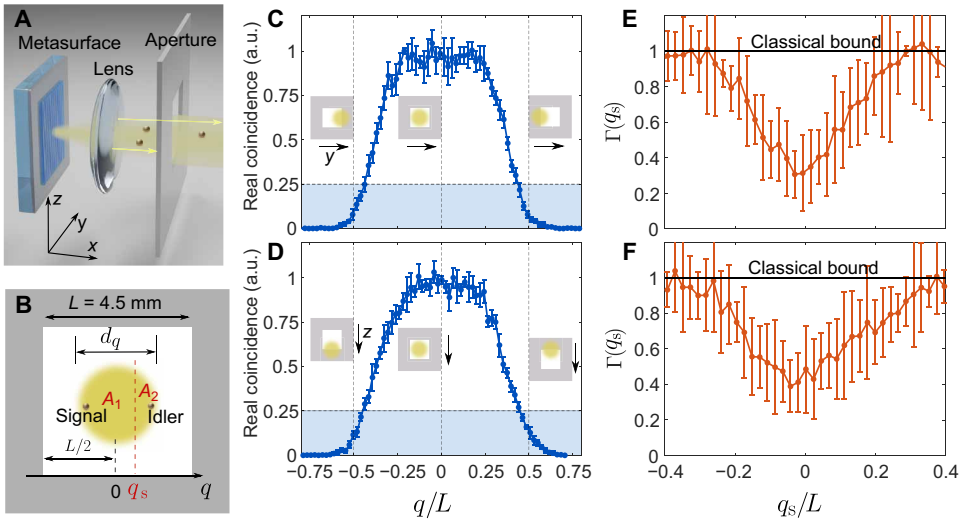

Fig. 4. Spatial entanglement of photon pairs. (**A**) Square aperture with a size of $L \times L$ (L = 4.5 mm) is introduced after the metasurface to characterize the spatial correlations of photon pairs. (**B**) The aperture size is larger than the profile of the collected beam determined by the size of the fiber collection lens. The position where the centers of the beam and the aperture are aligned is defined as zero. We characterize the correlations for the spatial regions A_1 and A_2 separated at the position q_s. (**C** and **D**) The real coincidence rate of collected photon pairs versus the aperture position along the y and z directions, normalized to the maximum value. The blue-shaded areas indicate the violation of CSI at $q = \pm L/2$. Error bars indicate 1 SD. (**E** and **F**) Violation of CSI for values below the classical bound. Error bars indicate 3 SD, corresponding to >99.7% confidence interval.

Let us estimate the degree of spatial antibunching for the case of $q_s = 0$, when half of the photons are blocked in either the horizontal or vertical direction (at $q = \pm L/2$ aperture positions). Then, for the photon emission with the spatial reflection symmetry following from the symmetric metasurface design, Eq. 2 simplifies to $\Gamma(0) = 4C(\pm L/2) \geq C(0)$. We see in Fig. 4 (C and D) that the coincidence rate drops by more than four times (within the area marked by shading) at $q = \pm L/2$, providing an additional visual confirmation of CSI violation. Specifically, the rate reduces by a factor of ~13 along the y (~6 along z) direction at $q = L/2$. The corresponding cross-correlations between the half-beam regions, which we estimate using eq. S23, are larger than the self-correlations by a factor of 5.5 for the y (~2 for z) direction, confirming the pronounced spatial antibunching.

These results demonstrate a noticeable difference between the emission directions. Specifically, the correlation function $\Gamma(q_s)$ values at $q_s = 0$ are 0.3 $C(0)$ and 0.5 $C(0)$ for the y and z directions, respectively. The larger CSI violation for the y direction agrees with the stronger antibunching estimated above. This suggests the presence of stronger spatial entanglement along the y compared to the z direction, which might be related to the off-normal emission of photons in the y direction according to the theoretical predictions shown in Fig. 1D.

DISCUSSION

In summary, we have proposed and experimentally demonstrated that enhanced generation of quantum photon-pair states can be facilitated through specially designed meta-gratings fabricated on top of a lithium niobate film with a subwavelength thickness. The metasurface supports nonlocal resonances that allow transverse phase matching of SPDC and the simultaneous control of the angular emission pattern over a broad pump wavelength tuning range, while the longitudinal matching requirements are removed because of an ultrasmall thickness. These unique features strongly enhance the photon-pair generation rate by over ~450 times compared to unpatterned structures, while the CAR reaches ~5000, demonstrating the high quality of quantum states. Our metasurface platform can lead to even higher photon rates and brightness by increasing the quality factor of optical resonances through improvements in the nanofabrication precision.

The generated photons can be strongly entangled in space while being almost indistinguishable in other degrees of freedom. In particular, we detect a purely linear polarization state of the photons with a high extinction ratio above 99%, which is achieved by designing the grating to selectively enhance the electric field component along the optical axis of the nonlinear film. On the other hand, theoretical modeling predicts a near-degenerate narrow emission spectrum of about ~3 nm. We experimentally characterized the spatial correlations of photon pairs by partially blocking the emission with an aperture and detected the violation of classical CSI, which serves as a criterion of spatial antibunching and multimode entanglement. We anticipate that future developments of this ultrathin platform, including the incorporation of inhomogeneous and two-dimensional meta-grating patterns, can allow even more flexibility in enhancing and shaping the photon emission and entanglement, paving the way toward various applications such as quantum imaging.

MATERIALS AND METHODS

Numerical simulations

The simulations of transmission spectra and eigenfrequencies are performed on the basis of the finite-element method by using the Comsol Multiphysics software package. The fitting of the CMT parameters and calculation of SPDC rate with CMT are done in MATLAB.

Metasurface fabrication

The designed metasurface was fabricated in a cleanroom starting from an $LiNbO_3$ film on quartz substrate from NANOLN. After ultrasonic cleaning, a thin layer of SiO_2 with a thickness of 200 nm was deposited on the sample by plasma-enhanced chemical vapor deposition. Then, polymethyl methacrylate (PMMA) was spin-coated as the resist for the subsequent electron beam lithography. After lithography, a thin layer of nickel with a thickness of 30 nm was coated by electron beam deposition followed by a lift-off process. The nickel pattern was used as the mask for etching of the SiO_2 layer by inductively coupled plasma etching. With the chemical of CHF_3 and pressure of 0.1 Pa, the etching rate was calibrated to be ~1.2 nm/s. Last, the residual nickel mask was removed by chemical etching. The size of the grating is 400 μm by 400 μm.

Second harmonic characterization

The femtosecond laser (Chameleon Compact OPO, Coherent) used to characterize the SHG from metasurface is set with the following parameters: beam diameter of ~100 μm, power of 10 mW, pulse width of 200 fs, linewidth of 23 nm, and repetition rate of 80 MHz. We use a lens with a focal length of 150 mm to focus the laser and an objective of 20× to collect the signal. The laser beam transmitting through the metasurface is removed with a short-pass filter before the signals are sent to the spectrometer.

SPDC experiments

The laser exciting the SPDC process is emitted from a Fabry-Perot laser diode (FPL785P, Thorlabs). The laser wavelength can be tuned from 780 to 790 nm, with a linewidth of ~0.1 nm. A short-pass filter at 850 nm before the metasurface and a long-pass filter at 1100 nm along with a band-pass filter at 1570 nm (with a 50-nm full width at half maximum) after metasurface suppress the fluorescence produced by the metasurface and other optics. Two lenses with a focal length of 100 mm are used to focus the pump beam and collimate the photons emitted from the metasurface. The photon pairs are collected with a multimode fiber and are probabilistically split into two optical paths with a 50:50 fiber beam splitter. The photons are registered with two single-photon detectors based on Indium gallium arsenide/Indium phosphide (InGaAs/InP) avalanche photodiodes (ID230, IDQ). The detection events are characterized by a time-to-digital converter (ID801, IDQ), whose coincidence window is set at 0.486 ns.

SUPPLEMENTARY MATERIALS

Supplementary material for this article is available at https://science.org/doi/10.1126/sciadv.abq4240

REFERENCES AND NOTES

1. R. Horodecki, P. Horodecki, M. Horodecki, K. Horodecki, Quantum entanglement. *Rev. Mod. Phys.* **81**, 865–942 (2009).
2. Y. H. Shih, Quantum imaging. *IEEE J. Sel. Top. Quantum Electron.* **13**, 1016–1030 (2007).
3. N. Gisin, R. Thew, Quantum communication. *Nat. Photon.* **1**, 165–171 (2007).
4. C. H. Bennett, D. P. DiVincenzo, Quantum information and computation. *Nature* **404**, 247–255 (2000).
5. D. N. Klyshko, Y. Sviridov, *Photons and Nonlinear Optics* (Gordon and Breach, 1988), p. 438.
6. K. W. Chan, J. P. Torres, J. H. Eberly, Transverse entanglement migration in Hilbert space. *Phys. Rev. A* **75**, 050101 (2007).
7. F. Just, A. Cavanna, M. V. Chekhova, G. Leuchs, Transverse entanglement of biphotons. *New J. Phys.* **15**, 083015 (2013).
8. A. Mair, A. Vaziri, G. Weihs, A. Zeilinger, Entanglement of the orbital angular momentum states of photons. *Nature* **412**, 313–316 (2001).
9. C. K. Law, J. H. Eberly, Analysis and interpretation of high transverse entanglement in optical parametric down conversion. *Phys. Rev. Lett.* **92**, 127903 (2004).
10. J. P. Torres, A. Alexandrescu, L. Torner, Quantum spiral bandwidth of entangled two-photon states. *Phys. Rev. A* **68**, 050301 (2003).
11. V. D. Salakhutdinov, E. R. Eliel, W. Löffler, Full-field quantum correlations of spatially entangled photons. *Phys. Rev. Lett.* **108**, 173604–173605 (2012).
12. C. Okoth, E. Kovlakov, F. Bonsel, A. Cavanna, S. Straupe, S. P. Kulik, M. V. Chekhova, Idealized Einstein-Podolsky-Rosen states from non-phase-matched parametric down-conversion. *Phys. Rev. A* **101**, 011801 (2020).
13. T. Huang, X. Zhao, S. Zeng, A. Crunteanu, P. P. Shum, N. Yu, Planar nonlinear metasurface optics and their applications. *Rep. Prog. Phys.* **83**, 126101 (2020).
14. C. De Angelis, G. Leo, D. N. Neshev, *Nonlinear Meta-Optics* (CRC Press, 2020), p. 344.
15. A. S. Solntsev, G. S. Agarwal, Y. Y. Kivshar, Metasurfaces for quantum photonics. *Nat. Photon.* **15**, 327–336 (2021).
16. A. I. Kuznetsov, A. E. Miroshnichenko, M. L. Brongersma, Y. S. Kivshar, B. Luk'yanchuk, Optically resonant dielectric nanostructures. *Science* **354**, aag2472 (2016).
17. G. Marino, A. S. Solntsev, L. Xu, V. F. Gili, L. Carletti, A. N. Poddubny, M. Rahmani, D. A. Smirnova, H. Chen, A. Lemaître, G. Zhang, A. V. Zayats, C. De Angelis, G. Leo, A. A. Sukhorukov, D. N. Neshev, Spontaneous photon-pair generation from a dielectric nanoantenna. *Optica* **6**, 1416–1422 (2019).
18. T. Santiago-Cruz, A. Fedotova, V. Sultanov, M. A. Weissflog, D. Arslan, M. Younesi, T. Pertsch, I. Staude, F. Setzpfandt, M. Chekhova, Photon pairs from resonant metasurfaces. *Nano Lett.* **21**, 4423–4429 (2021).
19. M. Parry, A. Mazzanti, A. Poddubny, G. Della Valle, D. N. Neshev, A. A. Sukhorukov, Enhanced generation of nondegenerate photon pairs in nonlinear metasurfaces. *Adv. Photon.* **3**, 055001 (2021).
20. B. Jin, D. Mishra, C. Argyropoulos, Efficient single-photon pair generation by spontaneous parametric down-conversion in nonlinear plasmonic metasurfaces. *Nanoscale* **13**, 19903–19914 (2021).
21. A. Mazzanti, M. Parry, A. N. Poddubny, G. Della Valle, D. N. Neshev, A. A. Sukhorukov, Enhanced generation of angle correlated photon-pairs in nonlinear metasurfaces. *New J. Phys.* **24**, 035006 (2022).
22. L. Michaeli, S. Keren-Zur, O. Avayu, H. Suchowski, T. Ellenbogen, Nonlinear surface lattice resonance in plasmonic nanoparticle arrays. *Phys. Rev. Lett.* **118**, 243904 (2017).
23. D. C. Hooper, C. Kuppe, D. Wang, W. Wang, J. Guan, T. W. Odom, V. K. Valev, Second harmonic spectroscopy of surface lattice resonances. *Nano Lett.* **19**, 165–172 (2019).
24. E. Klopfer, S. Dagli, D. Barton III, M. Lawrence, J. A. Dionne, High-quality-factor silicon-on-lithium niobate metasurfaces for electro-optically reconfigurable wavefront shaping. *Nano Lett.* **22**, 1703–1709 (2022).
25. A. Weiss, C. Frydendahl, J. Bar-David, R. Zektzer, E. Edrei, J. Engelberg, N. Mazurski, B. Desiatov, U. Levy, Tunable metasurface using thin-film lithium niobate in the telecom regime. *ACS Photonics* **9**, 605–612 (2022).
26. N. M. H. Duong, G. Saerens, F. Timpu, M. T. Buscaglia, V. Buscaglia, A. Morandi, J. S. Muller, A. Maeder, F. Kaufmann, A. Sonltsev, R. Grange, Broadband photon pair generation from a single lithium niobate microcube. arXiv:2109.08489 (2021).
27. S. Saravi, T. Pertsch, F. Setzpfandt, Lithium niobate on insulator: An emerging platform for integrated quantum photonics. *Adv. Opt. Mater.* **9**, 2100789 (2021).
28. D. Zhu, L. Shao, M. Yu, R. Cheng, B. Desiatov, C. J. Xin, Y. Hu, J. Holzgrafe, S. Ghosh, A. Shams-Ansari, E. Puma, N. Sinclair, C. Reimer, M. Zhang, M. Lončar, Integrated photonics on thin-film lithium niobate. *Adv. Opt. Photon.* **13**, 242–352 (2021).
29. A. Hessel, A. A. Oliner, A new theory of Wood's anomalies on optical gratings. *Appl. Optics* **4**, 1275–1297 (1965).
30. S. G. Tikhodeev, A. L. Yablonskii, E. A. Muljarov, N. A. Gippius, T. Ishihara, Quasiguided modes and optical properties of photonic crystal slabs. *Phys. Rev. B* **66**, 045102 (2002).
31. S. Fan, J. D. Joannopoulos, Analysis of guided resonances in photonic crystal slabs. *Phys. Rev. B* **65**, 235112 (2002).
32. X. Zhang, Q. Li, F. Liu, M. Qiu, S. Sun, Q. He, L. Zhou, Controlling angular dispersions in optical metasurfaces. *Light Sci Appl.* **9**, 76 (2020).
33. J.-H. Song, J. van de Groep, S. J. Kim, M. L. Brongersma, Non-local metasurfaces for spectrally decoupled wavefront manipulation and eye tracking. *Nat. Nanotech.* **16**, 1224–1230 (2021).
34. H. Kwon, D. Sounas, A. Cordaro, A. Polman, A. Alu, Nonlocal metasurfaces for optical signal processing. *Phys. Rev. Lett.* **121**, 173004 (2018).
35. S. S. Wang, R. Magnusson, Theory and applications of guided-mode resonance filters. *Appl. Optics* **32**, 2606–2613 (1993).
36. G. Quaranta, G. Basset, O. J. F. Martin, B. Gallinet, Recent advances in resonant waveguide gratings. *Laser Photon Rev.* **12**, 1800017 (2018).
37. C. W. Hsu, B. Zhen, A. D. Stone, J. D. Joannopoulos, M. Soljacic, Bound states in the continuum. *Nat. Rev. Mater.* **1**, 16048 (2016).
38. W. Suh, Z. Wang, S. Fan, Temporal coupled-mode theory and the presence of non-orthogonal modes in lossless multimode cavities. *IEEE J. Quantum Electron.* **40**, 1511–1518 (2004).

39. K. Sun, H. Jiang, D. A. Bykov, V. Van, U. Levy, Y. Cai, Z. Han, 1D quasi-bound states in the continuum with large operation bandwidth in the ω~k space for nonlinear optical applications. *Photon. Res.* **10**, 1575–1581 (2022).
40. J. Ma, J. Chen, M. Ren, W. Wu, W. Cai, J. Xu, Second-harmonic generation and its nonlinear depolarization from lithium niobate thin films. *Opt. Lett.* **45**, 145–148 (2020).
41. Z. Zhu, D. Zhang, F. Xie, J. Chen, S. Gong, W. Wu, W. Cai, X. Zhang, M. Ren, J. Xu, Infrared full-Stokes polarimetry by parametric up-conversion. arXiv:2110.10506 (2021).
42. K. H. Kim, W. S. Rim, Anapole resonances facilitated by high-index contrast between substrate and dielectric nanodisk enhance vacuum ultraviolet generation. *ACS Photonics* **5**, 4769–4775 (2018).
43. A. Fedotova, M. Younesi, J. Sautter, A. Vaskin, F. J. F. Lochner, M. Steinert, R. Geiss, T. Pertsch, I. Staude, F. Setzpfandt, Second-harmonic generation in resonant nonlinear metasurfaces based on lithium niobate. *Nano Lett.* **20**, 8608–8614 (2020).
44. L. Carletti, A. Zilli, F. Moia, A. Toma, M. Finazzi, C. De Angelis, D. N. Neshev, M. Celebrano, Steering and encoding the polarization of the second harmonic in the visible with a monolithic $LiNbO_3$ metasurface. *ACS Photonics* **8**, 731–737 (2021).
45. J. Ma, F. Xie, W. Chen, J. Chen, W. Wu, W. Liu, Y. Chen, W. Cai, M. Ren, J. J. Xu, Nonlinear lithium niobate metasurfaces for second harmonic generation. *Laser Photon Rev.* **15**, 2000521 (2021).
46. T. Wasak, P. Szankowski, M. Trippenbach, J. Chwedenczuk, Cauchy-Schwarz inequality for general measurements as an entanglement criterion. *Quantum Inf. Process.* **15**, 269–278 (2016).
47. A. Gatti, E. Brambilla, L. Lugiato, Chapter 5 quantum imaging. *Prog. Optics* **51**, 251–348 (2008).
48. R. Czaplicki, A. Kiviniemi, J. Laukkanen, J. Lehtolahti, M. Kuittinen, M. Kauranen, Surface lattice resonances in second-harmonic generation from metasurfaces. *Opt. Lett.* **41**, 2684–2687 (2016).
49. N. M. Tran, I. A. Chioar, A. Stein, A. Alekhin, V. Juve, G. Vaudel, I. Razdolski, V. Kapaklis, V. Temnov, Observation of the nonlinear Wood's anomaly on periodic arrays of nickel nanodimers. *Phys. Rev. B* **98**, 245425 (2018).
50. V. G. Kravets, A. V. Kabashin, W. L. Barnes, A. N. Grigorenko, Plasmonic surface lattice resonances: A review of properties and applications. *Chem. Rev.* **118**, 5912–5951 (2018).
51. A. N. Poddubny, D. N. Neshev, A. A. Sukhorukov, Quantum nonlinear metasurfaces, in *Nonlinear Meta-Optics*, C. D. Angelis, G. Leo, D. N. Neshev, Eds. (CRC Press, 2020), pp. 147–180.
52. R. R. Boye, R. K. Kostuk, Investigation of the effect of finite grating size on the performance of guided-mode resonance filters. *Appl. Optics* **39**, 3649–3653 (2000).
53. J. M. Bendickson, E. N. Glytsis, T. K. Gaylord, D. L. Brundrett, Guided-mode resonant subwavelength gratings: Effects of finite beams and finite gratings. *J. Opt. Soc. Am. A* **18**, 1912–1928 (2001).
54. C. Okoth, A. Cavanna, T. Santiago-Cruz, M. V. Chekhova, Microscale generation of entangled photons without momentum conservation. *Phys. Rev. Lett.* **123**, 263602 (2019).
55. T. Wasak, P. Szankowski, P. Zin, M. Trippenbach, J. Chwedenczuk, Cauchy-Schwarz inequality and particle entanglement. *Phys. Rev. A* **90**, 033616 (2014).
56. D. F. Walls, G. J. Milburn, *Quantum Optics, 2nd edition* (Springer, 2008).
57. I. N. Agafonov, M. V. Chekhova, G. Leuchs, Two-color bright squeezed vacuum. *Phys. Rev. A* **82**, 011801 (2010).
58. O. Jedrkiewicz, E. Brambilla, M. Bache, A. Gatti, L. A. Lugiato, P. Di Trapani, Quantum spatial correlations in high-gain parametric down-conversion measured by means of a CCD camera. *J. Mod. Opt.* **53**, 575–595 (2006).
59. K. V. Kheruntsyan, J. C. Jaskula, P. Deuar, M. Bonneau, G. B. Partridge, J. Ruaudel, R. Lopes, D. Boiron, C. I. Westbrook, Violation of the Cauchy-Schwarz inequality with matter waves. *Phys. Rev. Lett.* **108**, 260401 (2012).

Acknowledgments

Funding: We acknowledge the support by the Australian Research Council (DP190101559 and CE200100010). **Author contributions:** A.A.S., L.X., and D.N.N. developed the theoretical concept. J.Z. and M.P. performed the numerical modeling. J.Z. fabricated the sample and performed the linear transmission measurement. J.M., M.C., and R.C.-M. developed the experimental setup, performed the measurements, and processed the data. A.A.S. and D.N.N. supervised the project. All authors analyzed the results and cowrote the paper. **Competing interests:** The authors declare that they have no competing interests. **Data and materials availability:** All data needed to evaluate the conclusions in the paper are present in the paper and/or the Supplementary Materials.

Submitted 8 April 2022
Accepted 15 June 2022
Published 29 July 2022
10.1126/sciadv.abq4240